Computer-AidedDesign

Taylor & Francis
Taylor & Francis Group

Optimal tool orientation generation and chip volume/cutting force predictions for 5-axis CNC machining of curved surfaces using flat-end mills

Shan Luo [ID], Zuomin Dong [ID] and Martin B.G. Jun [ID]

University of Victoria, Canada

ABSTRACT

Machining using a flat-end mill with varying and optimal tool orientations and feed-rate is an ideal approach to reach the full potential of 5-axis CNC milling of curved surfaces. Rotating the flat-end mill with different tilt angles can produce different effective cutter curvatures at the cutter contact point (CCP), improving machining efficiency and surface quality with better cutter-workpiece curvature match, and avoiding gouging for concave surfaces. This CCP-focused approach, if combined with globally optimized CNC tool path and the optimal feed-rate determined by the constraining instant cutting force, present a systematic approach to optimize 5-axis CNC machining. However, this approach also presents significant challenges due to the complex tasks of modeling varying cutter and part surface geometry/interaction. This research is aimed at solving the stated research problem. Several new methods have been introduced for optimal tool orientation generation and for instant cutting chip volume and forces calculations. An optimal tool orientation generation method based on the combination of the surface normal method for convex curved surfaces and Euler-Meusnier Sphere (EMS) method for concave curved surfaces has been introduced to achieve the maximum machining efficiency and surface quality. A Non-uniform rational basis spline (NURBS) surface with concave, convex, and saddle features is used to demonstrate these newly introduced methods. After the optimal tool orientation is established, a Tri-dexel workpiece model is used to predict instant material removal rate and cutting forces by updating the machined workpiece and subtracting the cutter-workpiece engagement zone, to ultimately identify the maximum allowable feed-rate and depth of cut. The complex approach is verified separately at present. The geometry of the tool paths and machined surface was validated using machining simulations. A simplified cutting experiment using a 3-axis micro-milling machine is conducted to verify the predicted chip volume and cutting forces on a flat surface using a constant depth of cut and the pocket toolpath, and cutting force predictions are in good agreement with the measured data both in magnitude and trend if the runout effects are ignored.

1. Introduction

5-axis CNC machining is widely used to produce various components with complex curved surfaces while potentially providing better tool accessibility to complex surfaces, producing more accurate surface, increasing material removal rate, and reducing machine setup time [19].

Today, to avoid cutter-part surface interference/gouge at large curvature areas and to simplify toolpath/orientation planning, a small diameter ball-end mill is used during machining [29]. This leads to low machining efficiency and large cusps for areas of the surface with small curvature. Large diameter end cutters present a more rigid and capable tool with a varying cutter curvature from the radius of the cutter to infinity (in principle) to support better cutter-part curvature match, leading to

much improved machining efficiency and surface quality [8]. Therefore, it is more beneficial to use flat-end mills for curved surface machining and to plan to tool path and tool orientation with the best curvature match between the cutter and the machined surface at the cutter contact point (CCP). However, flat-end mills cannot easily avoid curvature gouging problems. It is still challenging to tool orientations using a flat-end cutter for sculptured surfaces without gouging generation in 5-axis CNC machining. There are some researches about the gouging avoidance. Du [31] proposes a method to detect and avoid gouging using a fillet-end milling cutter by exact curvature matching between the cutter and part surface. However, an initial inclination angle is required to obtain the minimum principal curvature of the cutter. If the minimum principal curvature of the cutter

CONTACT Shan Luo ✉ luoshan@uvic.ca; Zuomin Dong ✉ zdong@uvic.ca; Martin B. G. Jun ✉ zdong@uvic.ca

is less than the maximum principal curvature of the concave surface, the initial angle should be increased to avoid gouges. In this method, the tool needs to be adjusted until gouging is eliminated or reduced to a specified tolerance zone, which results in curvatures that are no longer matched and the effectiveness of the principal axis method is reduced at the CCP [11]. Rao [25] presents a mathematic method to detect and eliminate local gouging using flat-end tools by calculating curvature of the tool envelope surface. This method is limited to the machined surface and cannot be extended to other types of cutter [9]. The machining configuration space (C-space) which is the tool tilting and inclination parameter areas without gouging generation is used to find optimal tool orientations by different machining constraints [6,16,23]. This method considers local, rear, and global gouges in machining [13]. After construction of the C-space, there is an optimization process to select smaller tilt angles and the minimum changes of tool orientations. Although C-space is able to monitor all the possible tool orientations, it requires lots of computing time to reach the optimal solutions. The methods mentioned above can avoid gouges, however, only concave surfaces are considered. For a complex surface with concave, convex and saddle shapes, the machining efficiency cannot be the highest if only considers machining with gouge free. The closest curvature match and the longest cutting edge should also be considered to achieve the maximum machining efficiency and the surface quality.

After optimal CNC tool paths for the workpiece and the optimal 5-axis tool orientation for every point on the tool path are generated, the remaining machining parameters are the instant cutter feed-rate and cutting depth. The optimal or maximum allowable feed-rate and depth of cut for best productivity is constrained by the no-chatter maximum allowable cutting force. This, in turn, requires the accurate cutting chip volume and force estimates using the geometric model. There exist several methods to represent volumetric models in the NC simulation process, such as the voxel model and dexel model [26]. The dexel model represents an object with a grid of long columns compacted together extending along z-axis direction, while the voxel model consists of many small cubes in a regular lattice [32]. The difference between dexel and voxel model is the object of z-axis. In voxel model, the height of model is divided into many small pieces. For dexel model, the volume along z-axis is continuous without separating into pieces. Voxel representation has advantages in the Boolean operation over the dexel model because Boolean operations are conducted at the level of primitive volumetric element; but it is time consuming, since it requires data on every

solid cubes. The dexel model enables higher efficiency computation than the voxel model, as it does not require data on every section of model in z-axis direction which the voxel model has to consider [15]. There are many studies about the applications of dexel and voxel representations. Benouamer [2] presented multi-dexel model to do NC milling simulation. Every dexel includes values of entry and exit angles and the material property. But the multiple usage of the single-dexel model caused topological inconsistencies and ignored small objects if the size of dexel is too large. Hook [10] proposed a dexel data structure to simulate free-form. Each dexel is defined by ray intersection. However, in Hook's data, structure was limited to the viewing direction. The view cannot be changed once the dexel data structure has been built. Huang [12] improved Hook's approach by developing a Tri-dexel model to support dynamic viewing transformations and an assessment of dimension errors. The voxel model is robust and can apply to many CAD and NC simulation software [22]. Karunakaran [14] used octree solid representation which is an adaptive version of the voxel model to do the volumetric NC simulation. The voxel model was divided into eight parts recursively to simulate cutting process and optimize the cutting parameters to satisfy the cutting force constraints. Walstra [28] developed a 3D voxel structure to obtain removed volume from the raw stock in the prototyping system. The voxel representation used simple data structure to generate fast updating the workpiece. However, a huge memory space was required to storing the model data, if the accuracy of the model was improved by large size of voxels.

In this work, an optimal tool orientation based on the combination of the surface normal method for convex surfaces and the Euler-Meusnier Sphere (EMS) method for concave surfaces without surface gouge has been integrated to achieve the maximum removal material. After the optimal tool path is generated, instant cutting forces and cutting volume predictions are then considered to optimize feed rate and depth of cut to achieve high machining efficiency and surface quality in 5-axis CNC machining using flat-end mills. A Tri-dexel model sliced into many 2D laminated planes is applied to calculate cutting forces and chip volume.

2. Optimal tool orientation generation

The Euler-Meusnier Sphere (EMS) method, introduced previously by our research group [30], is method for calculating the curvatures of the machined surface and cutter surface at the CCP. The introduction of the general concept of EMS allows different types of milling cutters: spherical-end, flat-end, and torus-end to be considered
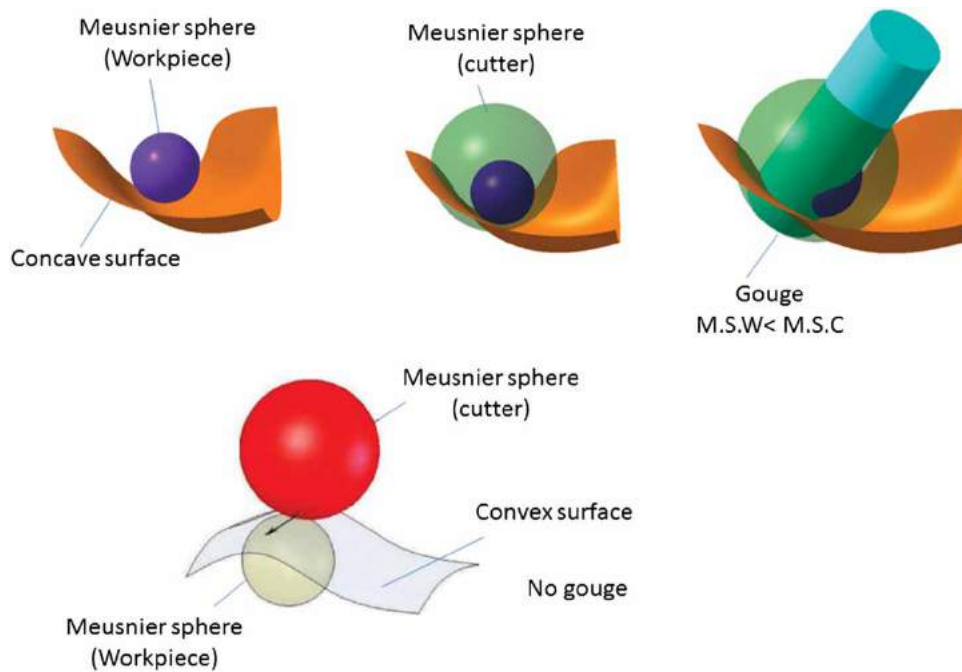
Figure 1. Machined surfaces and cutter Meusnier sphere.

using one model. A direct application of EMS is to ensure the effective curvature of the end milling cutter is large or equal than the curvature of the machined surface at the CCP, thus avoiding local gouging for concave surfaces. In execution, this is done by matching the largest EMS of the cutter with the smallest EMS of the machined surface at each CCP.

In Fig. 1, it can be seen that if the Meusnier sphere of cutter is larger than that of the workpiece, gouge would be generated. The EMS method provides a generic local solution for gouge detection and elimination in the end milling of concave surfaces. EMS also provides hints on the ideal rotational angles of 5-axis end and torus milling cutters to obtain best cutter-surface curvature match with improved machining efficiency and surface finish. For convex surfaces, the surface curvature and the tool curvature are opposite, no gouging will be generated. Surface normal direction presents the most efficient tool orientation for convex surface milling, since the largest Euler-Meusnier sphere or the longest cutting edge is generated at the surface normal direction with best cutter-surface curvature match. The EMS method works well for concave surfaces, while the surface normal method serves convex surfaces. A complex surface may consist of many surface patches in concave, convex or saddle shapes. The optimal tool orientation for 5-axis end milling can be obtained with the combination of the EMS and surface normal control methods to ensure better cutter-surface curvature match.

2.1. Two rotational angles identification by the EMS method

The criterion of the EMS method to avoid gouges is to match the largest cutter Meusnier sphere with the smallest Meusnier sphere of a surface at each CCP. In Fig. 2, P is the CCP, O is the center of smallest Meusnier sphere of the machined surface, A is the bottom center of the flat-end mill; $\vec{n}$ is the surface normal vector: $\vec{t}$ is the axis direction of the tool; OP is the radius of the smallest Meusnier Sphere of the workpiece, which is the reciprocal of the largest surface curvature at the CCP P, denoted by R; AP is the radius of the cutter, which is given as r. From
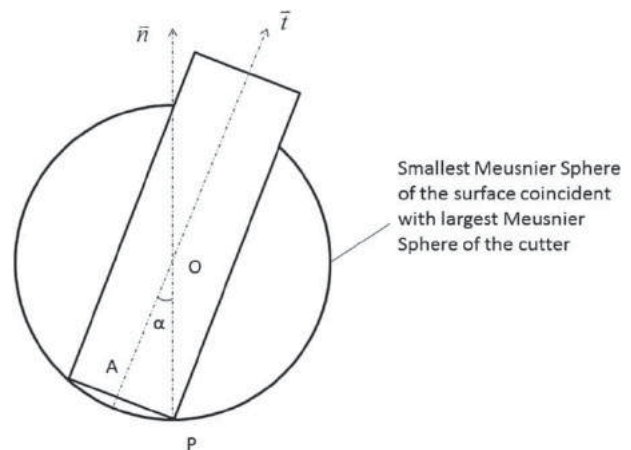
Figure 2. Inclination angle α confirmation.

the geometry of the cutter and the Meusnier sphere, the inclinational angle α can be obtained from the following equation:

$$\alpha = \sin^{-1}\left(\frac{r}{R}\right) \tag{2.1}$$

The radius of the smallest Meusnier sphere R is determined by the maximum surface curvature. Therefore, the surface maximum principle curvatures are required to get the inclination angle α. Radius of curvature is the reciprocal of the surface curvature at each cutter contact point. The maximal and minimal principal curvatures can be calculated by Gaussian and mean curvatures [17].

Curvature is used to describe how a surface changes its shape. Given a point on a surface, there are many normal curvatures at this point in various directions. The principal curvatures are the extremal curvature values, which are denoted by k_{min} and k_{max}. The maximum and minimum principal curvatures (k_{min} and k_{max}) are perpendicular. Both of them depend on the first and second partial derivatives of the surface. In mathematical terms, the directions and values of principal curvatures are the eigenvectors and the corresponding eigenvalues of the symmetric linear map L_P, which is based on the first and second fundamental forms.

In differential geometry, the first fundamental form is the inner product on the tangent space in 3-D Euclidean space [17]. For a surface S (u, v), the first fundamental form is denoted by I.

$$I = Edx^2 + 2Fdxdy + Gdy^2 \tag{2.2}$$

$$E = \langle S_u, S_u \rangle = |S_u|^2$$
$$F = \langle S_u, S_v \rangle = \langle S_v, S_u \rangle \tag{2.3}$$
$$G = \langle S_v, S_v \rangle = |S_v|^2$$

S_u and S_v are two tangent vectors on tangent space.

$$S_u = \frac{\partial S}{\partial u}, \quad S_v = \frac{\partial S}{\partial v} \tag{2.4}$$

The surface unit normal vector n is:

$$n = \frac{S_u \times S_v}{|S_u \times S_v|} \tag{2.5}$$

The coefficients of second fundament form at a given point are obtained by projections of second partial derivatives of S onto the normal line. They can be expressed by:

$$L = S_{uu} \cdot n, \ M = S_{uv} \cdot n, \ N = S_{vv} \cdot n \tag{2.6}$$

The matrixes of first and second fundamental form in the basis (S_u, S_v) of the tangent plane are I and II, respectively.

$$I = \begin{bmatrix} E & F \\ F & G \end{bmatrix}, \quad II = \begin{bmatrix} L & M \\ M & N \end{bmatrix} \tag{2.7}$$

A new matrix L_P called shape operator is formed to get the principal curvatures.

$$L_P = I^{-1}II \tag{2.8}$$

where, I^{-1} is the inverse matrix of I. The directions and values of principle curvatures are the eigenvectors and eigenvalues of the shape operator L_P.

Gaussian curvature and mean curvature are denoted by K and H, given by the following equations:

$$K = \frac{LN - M^2}{EG - F^2}, \quad H = \frac{EN + GL - 2FM}{2(EG - F^2)} \tag{2.9}$$

The maximum and minimal principal curvature K_{max} and K_{min} are obtained from Gaussian curvature and mean curvature:

$$K_{max} = H + \sqrt{H^2 - K}$$
$$K_{min} = H - \sqrt{H^2 - K} \tag{2.10}$$

The principal directions for maximum and minimal principal curvature are K_{dmax} and K_{dmin}, which expressed by:

$$K_{d\max} + K_{d\min} = -\frac{EN - GL}{FN - GM}$$
$$K_{d\max}K_{d\min} = \frac{EM - FL}{FN - GM} \tag{2.11}$$

The lead angle α has been determined by the largest surface curvature K_{max}. On the other hand, for better curvature match and machining efficiency, the tool axis should be in the plane A which is defined by the smallest principal curvature direction of the surface and the surface normal at the cutter contact point O, shown in Fig. 3.

From the relation of the tool axis, surface normal, and the smallest principal curvature direction shown in Fig. 3, it can be seen that the tool axis direction can be obtained once the minimal principal curvature direction K_{dmin} and the surface normal n at the cutter contact point O are confirmed. In Fig. 4, OC is the surface normal; OD is the minimal principal curvature direction at the point O, obtained from the Eqn. (2.11); OE is the tool axis expressed by t. γ is angle between surface normal and the minimal principal curvature direction. t is obtained by the Eqn. (2.12).

$$\overrightarrow{OE} = \overrightarrow{OC} + \overrightarrow{CE} = \overrightarrow{OC} + \frac{\alpha}{\gamma}(\overrightarrow{OD} - \overrightarrow{OC})$$
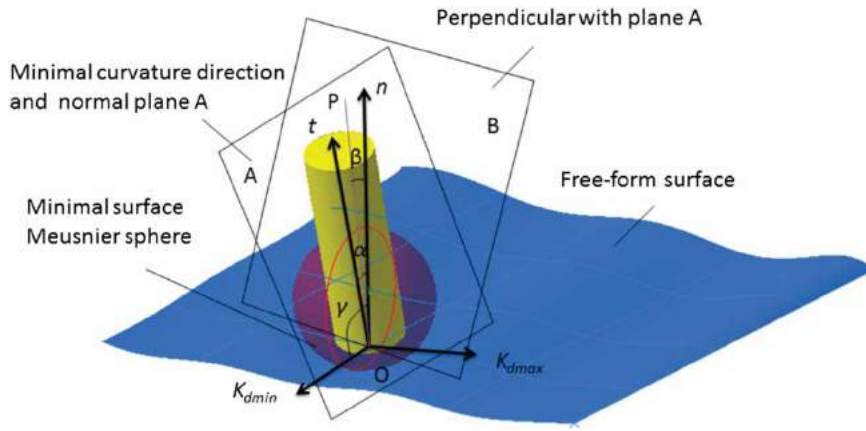$$= n + \frac{\alpha}{\gamma}(K_{d\min} - n) \tag{2.12}$$

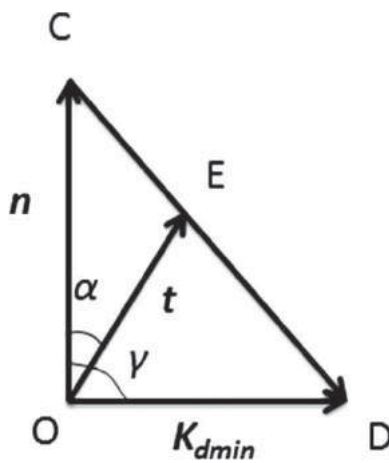**Figure 3.** Tool orientation in the Meusnier sphere method.

Figure 4. The relation of tool axis with the surface normal and the smallest principal curvature direction.

2.2. Optimal tool orientation

A NURBS surface is used in the paper to show optimal tool orientations in different surface features.

To find geometric parameters such as surface points, principal curvatures, and surface normal, the mathematical model of a NURBS surface is required. The surface equation is represented as [7,18]:

$$S(u, v) = \frac{\sum_{i=1}^{l+1} \sum_{i=1}^{m+1} h_{i,j} P_{i,j} N_{i,k}(u) N_{j,l}(v)}{\sum_{i=1}^{l+1} \sum_{i=1}^{m+1} h_{i,j} N_{i,k}(u) N_{j,l}(v)}$$
$$\times (u_{\min} \leq u \leq u_{\max}, v_{\min} \leq v \leq v_{\max})$$
$$(2.13)$$

where, u and v are two independent parameters, $P_{i,j}$ are the x, y, z coordinates and $h_{i,j}$ are a set of $(l+1)$ by $(m+1)$ control points in the homogeneous coordinates; $N_{i,k}$ and $N_{j,l}$ are the blending function in u and v directions.

The machined surface is roughly divided into concave, convex, and saddle shapes by Gaussian curvature and mean curvature [5]. The relationship between surface features and curvatures can be seen in the Tab. 1.

For a concave shape, Gaussian curvature is positive and mean curvature is negative; for a convex shape, both Gaussian and mean curvatures are positive. A saddle shape is special with curves up in one direction, and curves down in a different direction. It means saddle points can become concave points and convex points by different machining directions. For instance, in Fig. 5(a), a NURBS surface consists of three surface features: concave (cyan squares), convex (pink stars), and saddle (blue circles). It can be seen that saddle points in Fig. 5(a) are concave points if machining the surface along u direction and they are convex ones if machining along v direction.

The tool orientation methods are then selected once the surface features, curvatures, and machining direction are determined. For convex shapes, surface normal at each convex point is the best choice for the tool orientation with the highest machining efficiency and without gouges generation. For concave shapes, EMS method is used to avoid gouging problems for flat-end mills. Tool orientations for saddle shapes can be applied to the surface normal variable control method and the EMS method depending on the selected machining direction.

Table 1. Relations of surface features, curvatures, gouging and the tool orientation methods.

| Surface features	Gaussian curvature $C_{Gaussian}$	Mean curvature C_{mean}	Gouging possibility	Tool orientation methods
Concave	$C_{Gaussian} > 0$	$C_{mean} < 0$	Certain	EMS
Convex	$C_{Gaussian} > 0$	$C_{mean} > 0$	Impossible	Surface normal
Saddle	$C_{Gaussian} < 0$	$C_{mean} < 0/C_{mean} > 0$	Uncertain	EMS/Surface normal
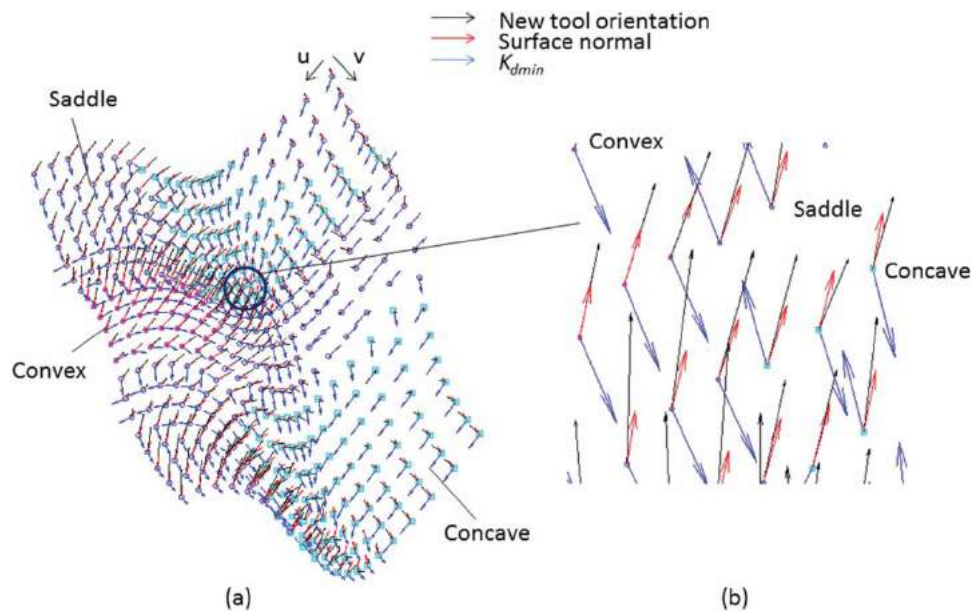
Figure 5. (a) Optimal tool orientations for the NURBS surface, (b) Display of the new tool orientations, surface normal, and minimal surface curvature directions.

Fig. 5(a) shows optimal tool orientations by the combination of the EMS and surface normal methods for a NURBS surface. Saddle points are considered as concave points as the toolpath is along *u* direction. In Fig. 5(b), black arrows denote new tool orientations. It may be surface normal or the tool axis in the EMS method. Red arrows represent surface normal vectors and blue arrows are the minimal principal curvature directions.

3. The tri-dexel method of chip volume and cutting force predictions for free-form surfaces

In this work, an improved Tri-dexel model (shown in Fig. 6) is applied as a workpiece model defined by many rectangles extending along the z-axis. Tri-dexel locations are confirmed by a 2D grid in the xy-plane and physically extend the z-axis of the Tri-dexel coordinate system. Grid points are uniformly distributed along x, y and z axes by distances *dx*, *dy*, and *dz* respectively. The size of each Tri-dexel cube *dx*, *dy*, and *dz* are determined by a user specified tolerance. The higher the tolerance, the more accurate calculation of chip volume and cutting forces there will be. However, high tolerance causes long computing time. To resolve this problem, the regular Tri-dexel mode is improved by slicing the Tri-dexel workpiece into many 2D laminated planes. All Boolean intersections and subtractions are performed on the laminated planes and the plane heights are given by user. In the Tri-dexel model, each slice shares the same height information. It is unnecessary to store the
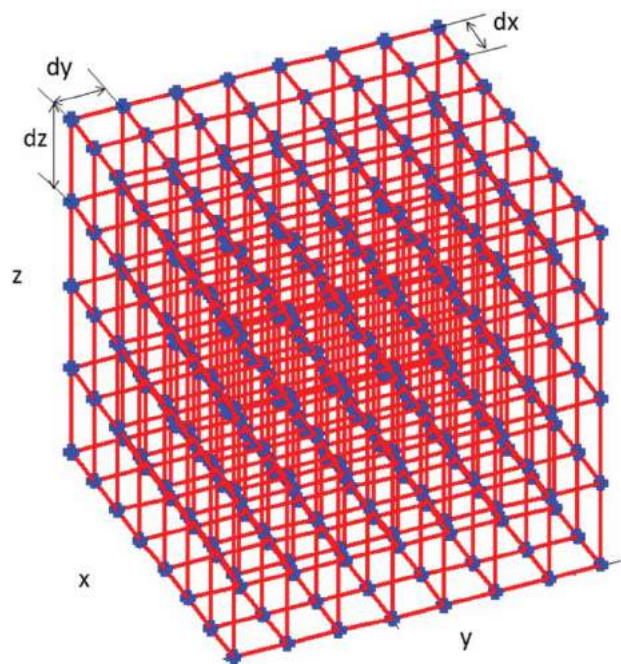
Figure 6. The Tri-dexel workpiece model in 3D.

data of height information for every Tri-dexel cell which could save storage memory and generate fast updating workpiece. Vertices in the Tri-dexel workpiece model are the blue points shown in Fig. 6. Line segments between two neighboring vertices can be obtained through the given locations of vertices. The Boolean subtraction of cutter volumes from the workpiece is equivalent to removed line segments which are located inside the cutter envelope.

3.1. Chip volume model

3.1.1. Tool projections on the tri-dexel workpiece

To reduce the complexity of 3D Boolean subtraction, 2D laminated planes Boolean subtraction is used by combining all planes along z-axis direction. The Tri-dexel model of the workpiece is divided into many layers. The number of layers depends on the depth of cut and the resolution defined by user. On each layer, it consists of m by n grid points. The number of layers is depended on the tolerance defined by user. Chip volume and cutting forces are relative to chip thickness, obtained by moving the tool along a distance of feed per tooth. To simulate the machining process and find chip thickness, a layer of the workpiece is used to display the generation of chip thickness and the Boolean subtraction. The projection of a flat-end mill on a plane is an ellipse. The ellipse is relative to two neighboring NC points, which are denoted by $(x_{i-1}, y_{i-1}, z_{i-1}, \alpha_{i-1}, \beta_{i-1})$ and $(x_i, y_i, z_i, \alpha_i, \beta_i)$. The equations of the ellipse at the ith NC point can be obtained from [20]:

$$X_{iellipse} = r \cos\theta \cos\beta_i - r \sin\theta \sin\beta_i \cos\alpha_i$$
$$+ \sin\beta_i \sin\alpha_i \frac{h_i - r\sin\theta \sin\alpha_i - \triangle z_i}{\cos\alpha_i} + \triangle x_i$$
$$(3.1)$$

$$Y_{iellipse} = r\cos\theta \sin\beta_i + r\sin\theta \cos\beta_i \cos\alpha_i$$
$$- \cos\beta_i \sin\alpha_i \frac{h_i - r\sin\theta \sin\alpha_i - \triangle z_i}{\cos\alpha_i} + \triangle y_i$$
$$(3.2)$$

$$Z_{iellipse} = |h_i|(Z_{\min} \le h_i \le 0) \qquad (3.3)$$

where, r is the tool radius, θ is the immersion angle, α_i is lead angle, β_i is tilt angle, h_i is the height of the plane, $\triangle x_i$

and $\triangle y_i$ are translation steps along x and y axes at the ith NC point.

3.1.2. Boolean operation and chip thickness generation

The simulation of cutting process is equivalent to the Boolean subtraction of tool volumes from the machined workpiece. Fig. 7 shows chip thickness generation and the 2D Boolean subtraction. As the tool moves from the previous position P_0 to current position P_1, new intersections of the Tri-dexel workpiece and current tool's boundary are found and stored in the current list. They are denoted by $C_1, C_2 \ldots C_j$, j is the number of intersections. Line segments which run from the current tool center to the points from current list are connected to get the intersections with the previous tool edge. These intersections are stored in the previous list, denoted by P_1, $P_2 \ldots P_j$. From here, a polyline arc-shape along the tool edge is generated by connecting intersections in the previous and current lists. The polyline arc-shape is regarded as the chip area on each slice. It can be calculated by adding all areas of small polygons, such as the polygon $C_1 C_2 P_1 P_2$ show in Fig. 7. As the polygons are very small, they can be considered as rectangles to calculate the area.

On the kth removal chip slice, the chip area A_k is obtained by the accumulating of many small polygons C_j $C_{j+1} P_{j+1} P_j$, j is the number of intersections in the current list. The chip area A_k can be got from the following equation:

$$A_k = \sum_{j=1}^{N} (C_j C_{j+1} \times P_{j+1} C_{j+1}) \qquad (3.4)$$

where, $C_j C_{j+1}$ is the integrated tool edge length, $P_{j+1} C_{j+1}$ is the chip thickness t_{j+1}.
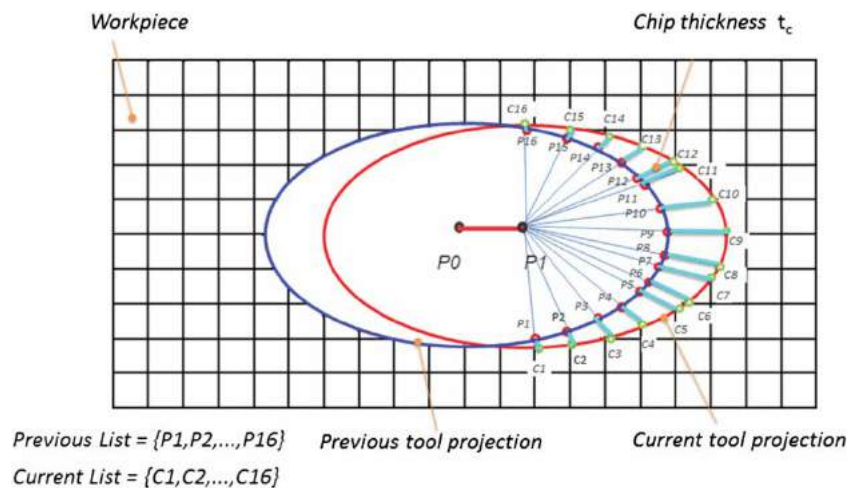

Previous List = {P1,P2,...,P16}   Previous tool projection   Current tool projection
Current List = {C1,C2,...,C16}

Figure 7. Boolean subtraction and chip thickness generation in the Tri-dexel workpiece.

The material in the polyline arc-shape is removed. From the geometry of the tool and the workpiece, it can be seen that workpiece line segments which are inside the current tool projection are trimmed. Therefore, the problem becomes finding entities that are inside an ellipse and then deleting line segments composed by these entities. Points inside an ellipse can be obtained by the following inequality:

$$\frac{x^2}{a^2} + \frac{y^2}{b^2} \leq 1 \quad (3.5)$$

where, a and b are the semi-major axis and semi-minor axis of an ellipse of the current tool projection.

Lines connected by points from current and previous lists are chip thickness, denoted by $C_j P_j$ in Fig. 7. Chip thickness can be obtained once the intersections of the workpiece and current and previous tool edges are determined. Let (x_{cj}, y_{cj}, z_{cj}) be the coordinates at the current tool projection point C_j; (x_{pj}, y_{pj}, z_{pj}) represents the coordinates of the previous tool projection point P_j. The chip thickness t_j in the 3D Euclidean space is:

$$t_j = \sqrt{(x_{cj} - x_{pj})^2 + (y_{cj} - y_{pj})^2 + (z_{cj} - z_{pj})^2} \quad (3.6)$$

Fig. 8 shows the same method can be used to get chip thickness on different layers. The chip volume and cutting force calculation can be calculated by chip thickness.
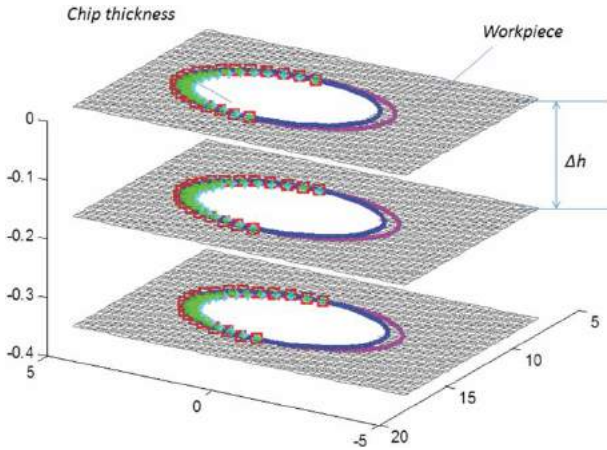
Figure 8. Chip thickness on the Tri-dexel workpiece.

3.1.3. Chip volume calculation

It is essential to continually subtract the intersections of the tool at two adjacent motions from the raw stock in order to get a final chip shape and predict cutting forces as realistically as possible. Chip thickness is updated and removed by every tool milling along the feed direction. The removal volume can be thought of as the Boolean intersections of the tool envelope with the workpiece. To get the chip volume, the workpiece is firstly divided into many parallel slices. Fig. 8 shows the slice volume on the Tri-dexel workpiece; the chip area and chip thickness are then calculated on each slice from Eqn. (3.4) and Eqn. (3.6). Finally, total chip volume at the ith NC point is obtained by accumulating all chip areas from layers by Eqn. (3.7).

$$V_i = \sum_{k=1}^{M} \sum_{j=1}^{N} C_j C_{j+1} \times P_{j+1} C_{j+1} \times \Delta h \quad (3.7)$$

where, Δh is the integrating height, i is the number of NC points, j is the number of cutter-workpiece intersections on each slice, k is the number of slices.

Fig. 9(a) shows cutter-workpiece engagement by layers; Fig. 9(b) illustrates that the chip shape consists of many non-uniform distributed polygons. This is due to line segments from P_1 to the current tool edge (shown in Fig. 7) not being uniformly distributed, causing non-uniform distributed immersion angles.

An example of cutter profiles at some tool motions illustrates the changed depth of cut, shown in the Fig. 10. There are three cases for depth of cut affecting number of layers of the workpiece. Firstly, if the depth of cut increases, a new layer of the workpiece without any subtraction operation is added to the workpiece at the previous tool motion. Subtraction would be operated in the new layer of the workpiece, and information of line segments are saved for the next tool operation. If the depth of cut does not change too much, the numbers of workpiece layers are the same as the last tool motion. Finally, if the depth of cut decreases, only part of the workpiece would participate in Boolean intersecting and subtracting operations; line segments in the participated workpiece are updated after every Boolean operation. The other layers of the workpiece at the previous tool motion, whose heights are larger than the maximum height of the tool at current position, would not perform the Boolean operation until the depth of cut is bigger than its maximum height.

Fig. 11 shows the simulation of the tool is removing material from the workpiece. It can be seen that the density of the removed workpiece is different which is due to the depth of cut changing for the whole toolpath.
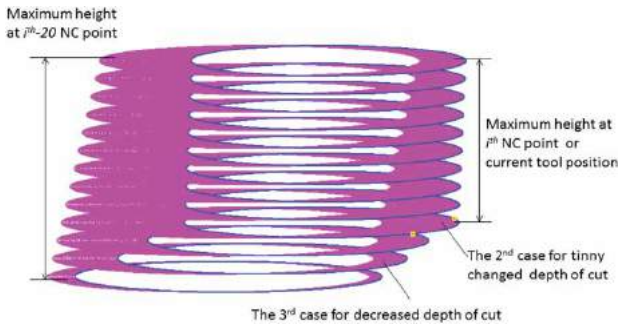
3.2. Cutting forces prediction

For a given NC point on the flat-end milling, the three differential cutting forces radial (F_r), axial (F_a) and tangential (F_r) are given by the following equation [4,21,24]:

$$dF_r = (K_{rc} \times t_j + K_{re}) \times dz$$
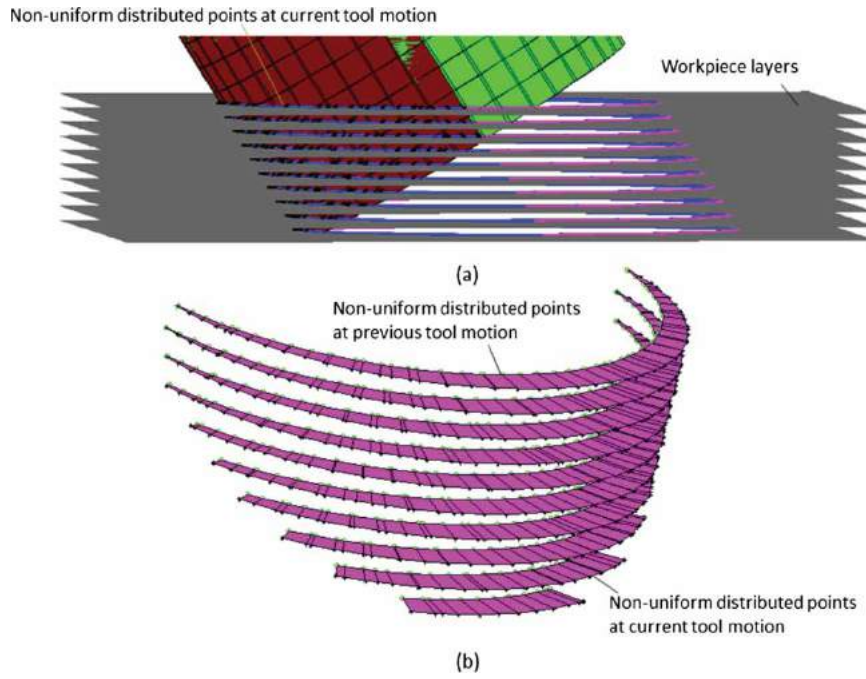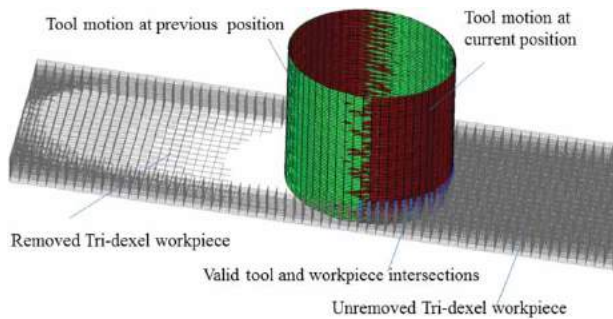
Figure 9. The non-uniform distributed chip shape.

Figure 10. Varied depth of cut in the workpiece method.

Figure 11. Cutting simulation of tool removing in the Tri-dexel workpiece.

$$dF_a = (K_{ac} \times t_j + K_{ae}) \times dz \qquad (3.8)$$
$$dF_t = (K_{tc} \times t_j + K_{te}) \times dz$$

where, K_{rc}, K_{ac}, and K_{tc} are the radial, axial, and tangential cutting force coefficients, and K_{re}, K_{ae}, and K_{te} are the edge force coefficients, determined by experimental tests and the workpiece material properties. t_j is the instantaneous undeformed chip thickness given in Eqn.(3.6); dz is the integrating height along z-axis.

In the feed coordinate system, cutting forces are obtained by transforming the differential radial, axial, and tangential forces using the immersion angle ϕ:

$$dF_x = -dF_t \cos \phi_{i,k} - dF_r \sin \phi_{i,k}$$
$$dF_y = dF_t \sin \phi_{i,k} - dF_r \cos \phi_{i,k} \qquad (3.9)$$
$$dF_z = dF_a$$

Finally, differential forces in the feed coordinate system are summed for all layers in a toolpath segment.

4. Experimental verification

A benchmark experiment [1] has been used to verify the simulation cutting force and chip volume modeling methods on a flat surface with the pocket toolpath (shown in Fig. 12). The depth of cut is 0.2 mm. The experiment was conducted in a 3-axis ALIO micro-milling machine with a spindle speed of 30,000 rpm and a feed rate of 1 μm/tooth. A four-flute flat-end mill with a diameter of 2 mm was used to cut an AL 6061 workpiece in the air without lubricant. The size of the workpiece is 10 × 15 × 5 mm as the width, length, and height, respectively. The benchmark data is collected by a 3-axis Kistler table dynamometer (MiniDyn 9256C1). The
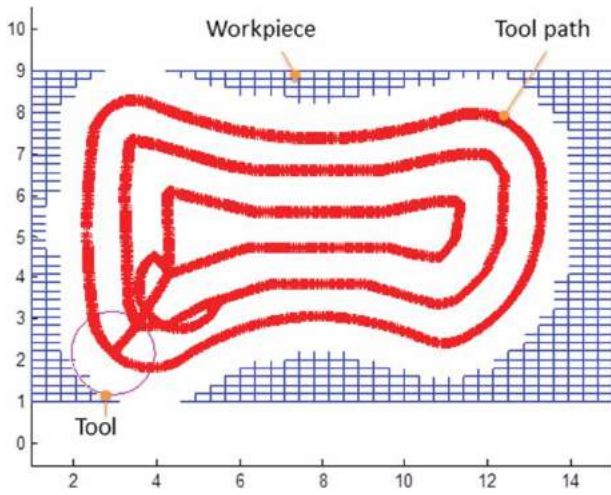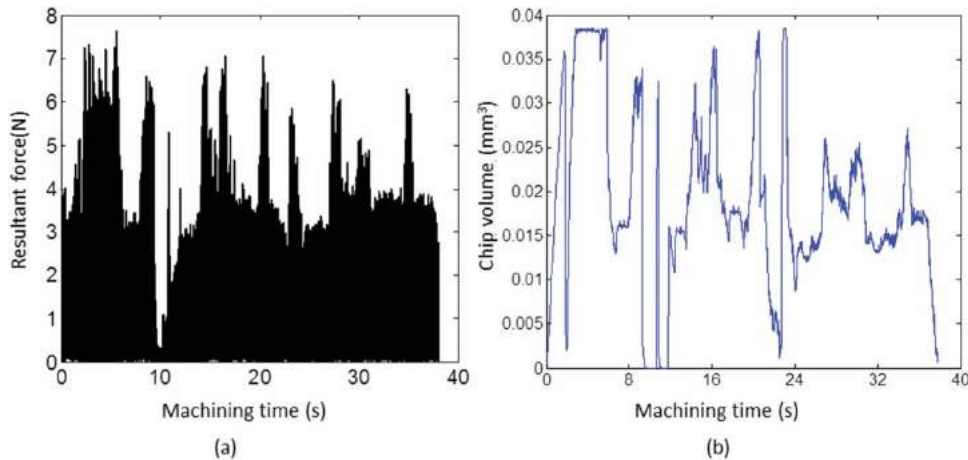
Figure 12. The pocket toolpath.

5-axis cutting forces modeling method based on the Tri-dexel workpiece can also work in 3-axis milling with the two rotational angles set to be zero.

Resultant cutting force acting on the tool is obtained by:

$$R = \sqrt{F_x{}^2 + F_y{}^2 + F_z{}^2} \qquad (4.1)$$

Fig. 13(a) illustrates the measured resultant force changed with machining time, while Fig. 13(b) shows the chip volume changed with machining time. From the comparison, it can be seen that the trend of chip volume was similar to the experimental resultant cutting force. The calculation of chip volume is faster and easier than cutting force. Therefore, chip volume is significant parameter to choose optimal cutting parameters such as feed rate, depth of cut, and spindle speed in the machining process planning.

On PC with a 3.6 GHz Pentium central processing unit (CPU) and 8GB of RAM, it took around 5 minutes for the simulation of cutting forces and chip volume calculation. The simulation time depends on the grid size of the Tri-dexel model. The smaller the grid size, the longer computing time there will be. Fig. 14 shows the comparison of predicted and measured cutting forces for machining the whole flat surface. The broken green line is the simulation resultant cutting force, and the black line is the experimental resultant force. The predicted resultant cutting force was accurately predicted by the cutting coefficients generated from the experiment tests. The trend and magnitudes of estimated resultant cutting force were in reasonably good agreement to the measured force if the runout problems are ignored.
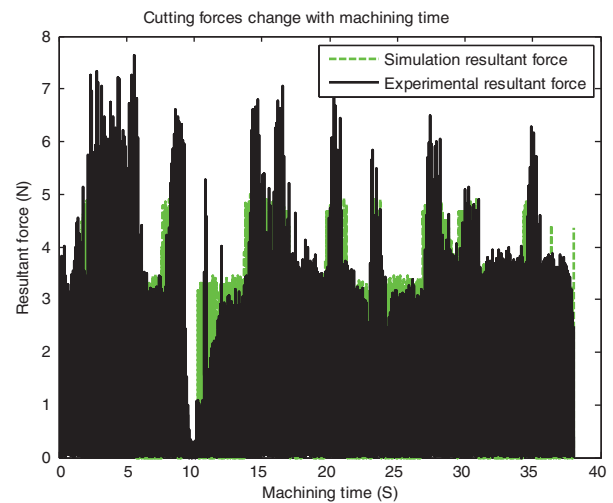
Figure 14. Comparison of simulation and experimental resultant forces in 3-axis milling.

At present, cutting force calculation for 5-axis ball-end milling is normally done using analytical method

Figure 13. (a) Measured resultant cutting forces changing with machining time; (b) Predicted chip volume changing with machining time.

[3,27]. It is relatively easy to calculate the intersections of a ball-end mill at different positions due to its constant cutter curvature. For 5-axis CNC milling using a flat-end cutter, the chip thickness and cutting force are difficult to calculate analytically due to the complexity of cutter-part geometry and the fact that the effective curvature of the cutter at the CCP is always changing with different cutter rotation angles. The proposed Tri-dexel method allows the chip thickness and cutting force to be calculated for flat-end milling using a numerical approach, but it requires more computation time to carry out these calculations.

5. Conclusion

An optimal tool orientation method that combines the Euler-Meusnier Sphere (EMS) and surface normal variable control approaches is proposed to improve machining efficiency and avoid gouges in a 5-axis CNC machine using a flat-end mill. The surface normal based cutter orientation planning method is used to obtain the closest curvature match and longest cutting edge; and the EMS method is applied to obtain the closest curvature match and to avoid local gouging by matching the largest cutter Euler-Meusnier sphere with the smallest Euler-Meusnier sphere of the machined surface at each cutter contact (CC) point. For surfaces with saddle shapes, selection of one of these two tool orientation determination methods is based on the direction of the CNC toolpath relative to the change of surface curvature. A Tri-dexel workpiece model is generated to predict removal material volume and cutting force by updating the machined workpiece and subtracting the cutter-workpiece engagement zone. The 3D Tri-dexel workpiece is sliced into many 2D laminated layers to reduce the complexity of 3D Boolean operations. On each slice, the instantaneous chip thickness is determined by the intersections of the tool cutting edge and the workpiece line segments. Simulations of cutting forces and chip volume for 5-axis milling have been carried out by the Tri-dexel workpiece method. The new approach has been verified using 5-axis CNC milling simulations and simplified 3-axis machining experiments. Cutting force model validation experiments in controlled cutting conditions have been carried out on a 3-axis micro CNC machine. The simulated results were in reasonably good agreement with the experiment cutting forces.

Acknowledgements

ORCID

Shan Luo http://orcid.org/0000-0003-4116-7213
Zuomin Dong http://orcid.org/0000-0001-7149-8422
Martin B.G. Jun http://orcid.org/0000-0002-0512-7209

References

[1] Bayesteh, A.; Jun, M. B.-G.: Feed rate optimization issues in micro-milling, in Proceedings of NAMRI/SME, 2013.

[2] Benouamer, M. O.; Michelucci, D.: Bridging the gap between CSG and Brep via a triple ray representation, in Proceedings of the fourth ACM symposium on Solid modeling and applications, 1997, Atlanta, Georgia, USA, ACM. http://dx.doi.org/10.1145/267734.267755.

[3] Bouzakis, K. D.; Aichouh, P.; Efstathiou, K.: Determination of the chip geometry, cutting force and roughness in free form surfaces finishing milling, with ball end tools, International Journal of Machine Tools and Manufacture, 43(5), 2003, 499–514. http://dx.doi.org/10.1016/S0890-6955(02)00265-1.

[4] Budak, E.; Ozturk, E.; Tunc, L. T.: Modeling and simulation of 5-axis milling processes, CIRP annals, 58(1), 2009, 347–350. http://dx.doi.org/10.1016/j.cirp.2009.03.044.

[5] Chen, Z. Z.; Dong, Z. M.; Vickers, G. W.: Automated surface subdivision and tool path generation for 3 1/2 1/2-axis CNC machining of sculptured parts, Computers in Industry, 50(3), 2003, 319–331. http://dx.doi.org/10.1016/s0166-3615(03)00019-8.

[6] Chiou, C. J.; Lee, Y. S.: A shape-generating approach for multi-axis machining G-buffer models, Computer-Aided Design, 31(12), 1999, 761–776. http://dx.doi.org/10.1016/S0010-4485(99)00069-X.

[7] Chiou, J. C. J.; Lee, Y.-S.: Five-Axis High Speed Machining of Sculptured Surfaces by Surface-Based NURBS Path Interpolation, Computer-Aided Design and Applications, 4(5), 2007, 639–648. http://dx.doi.org/10.1080/16864360.2007.10738498.

[8] Fard, M. J. B.; Feng, H. Y.: Effect of tool tilt angle on machining strip width in five-axis flat-end milling of free-form surfaces, International Journal of Advanced Manufacturing Technology, 44(3–4), 2009, 211–222. http://dx.doi.org/10.1007/s00170-008-1828-3.

[9] Gong, H.; Cao, L.-X.; Liu, J.: Second order approximation of tool envelope surface for 5-axis machining with single point contact, Computer-Aided Design, 40(5), 2008, 604–615. http://dx.doi.org/10.1016/j.cad.2008.02.003.

[10] Hook, T. V.: Real-time shaded NC milling display, SIGGRAPH Comput. Graph., 20(4), 1986, 15–20. http://dx.doi.org/10.1145/15886.15887.

[11] Hosseinkhani, Y.; Akbari, J.; Vafaeesefat, A.: Penetration-limination method for five-axis CNC machining of sculptured surfaces, International Journal of Machine Tools & Manufacture, 47(10), 2007, 1625–1635. http://dx.doi.org/10.1016/j.ijmachtools.2006.11.002.

[12] Huang, Y.; Oliver, J. H.: NC milling error assessment and tool path correction, in Proceedings of the 21st annual conference on Computer graphics and interactive techniques, 1994: ACM. http://dx.doi.org/10.1145/192161.192231.

[13] Jun, C. S.; Cha, K.; Lee, Y. S.: Optimizing tool orientations for 5-axis machining by configuration-space search method, Computer-Aided Design, 35(6), 2003, 549–566. http://dx.doi.org/10.1016/s0010-4485(02)00077-5.

[14] Karunakaran, K. P.; Shringi, R.: A solid model-based off-line adaptive controller for feed rate scheduling for milling process, Journal of Materials Processing Technology, 204(1), 2008, 384–396. http://dx.doi.org/10.1016/j.jmatprotec.2007.11.092.

[15] Lee, S.; Nestler, A.: Virtual workpiece: workpiece representation for material removal process, The International Journal of Advanced Manufacturing Technology, 58(5–8), 2012, 443–463. http://dx.doi.org/10.1007/s00170-011-3431-2.

[16] Li, S. X.; Jerard, R. B.: 5-axis machining of sculptured surfaces with a flat-end cutter, Computer-Aided Design, 26(3), 1994, 165–178. http://dx.doi.org/10.1016/0010-4485(94)90040-X.

[17] Li, X.: Curvature analysis and geometric description of landforms using MATLAB, in Environmental Science and Information Application Technology (ESIAT), 2010, Wuhan.

[18] Liang, H. B.; Li, X.: A 5-axis Milling System Based on a New G code for NURBS Surface, 2009 IEEE International Conference on Intelligent Computing and Intelligent Systems, Proceedings, Vol 2, ed. W. Chen, S.Z. Li, and Y.L. Wang. 2009, 5. 600–606.

[19] Lin, T.; Lee, J. W.; Bohez, E. L. J.: A new accurate curvature matching and optimal tool based five-axis machining algorithm, Journal of Mechanical Science and Technology, 23(10), 2009, 2624–2634. http://dx.doi.org/10.1007/s12206-009-0724-6.

[20] Luo, S.; Dong, Z.; Jun, M. B. G.: Chip volume calculation and simulation in 5-axis CNC machining with flat-end mill, in Virtual Machining Process Technology conference, 2015.

[21] Makhanov, S. S.; Anotaipaiboon, W., Advanced Numerical Methods to Optimize Cutting Operations of Five-Axis Milling Machines, 5, Editor. 2007, Springer Series in Advanced Manufacturing.

[22] Muller, H., et al.: Online sculpting and visualization of multi-dexel volumes, in Proceedings of the eighth ACM symposium on Solid modeling and applications, 2003, Seattle, Washington, USA: ACM. http://dx.doi.org/10.1145/781606.781646.

[23] Olling, G., et al., Five-axis Control Sculptured Surface Machining Using Conicoid End Mill, in Machining Impossible Shapes. 1999, Springer US. p. 366–375.

[24] Ozturk, E.; Budak, E.: Modeling of 5-axis milling processes, Taylor & Francis Group, 11, 2007, 287–311.

[25] Rao, A.; Sarma, R.: On local gouging in five-axis sculptured surface machining using flat-end tools, Computer aided design, 32(2000), 2000, 409–420.

[26] Ren, Y.; Lai-Yuen, S. K.; Lee, Y.-S.: Virtual prototyping and manufacturing planning by using Tri-dexel models and haptic force feedback, Virtual and Physical Prototyping, 1(1), 2006, 3–18. http://dx.doi.org/10.1080/17452750500283590.

[27] Sonawane, H. A.; Joshi, S. S.: Analytical modeling of chip geometry and cutting forces in helical ball end milling of superalloy Inconel 718, CIRP Journal of Manufacturing Science and Technology, 3(3), 2010, 204–217. http://dx.doi.org/10.1016/j.cirpj.2010.11.003.

[28] Walstra, W. H.; Bronsvoort, W. F.; Vergeest, J. S. M.: Interactive simulation of robot milling for rapid shape prototyping, Computers & Graphics, 18(6), 1994, 861–871. http://dx.doi.org/10.1016/0097-8493(94)90013-2.

[29] Wang, Y. J., Curvature Gouge Detection and Prevention in 5-axis CNC Machining 2007.

[30] Wang, Y. J.; Dong, Z.; Vickers, G. W.: Euler-Meusnier Sphere Based Milling Cutter Model for Curvature Gouge Avoidance in Curved Surface Machining, Society of Manufacturing Engineers, 2008, 1–9.

[31] Weinert, K., et al.: Swept volume generation for the simulation of machining processes, International Journal of Machine Tools and Manufacture, 44(6), 2004, 617–628. http://dx.doi.org/10.1016/j.ijmachtools.2003.12.003.

[32] Zhu, W.; Lee, Y.-S.: Dexel-based force-torque rendering and volume updating for 5-DOF haptic product prototyping and virtual sculpting, Computers in Industry, 55(2), 2004, 125–145. http://dx.doi.org/10.1016/j.compind.2004.07.003.